Journal of Solid State Chemistry 184 (2011) 2877–2886

Contents lists available at SciVerse ScienceDirect

Journal of Solid State Chemistry

journal homepage: www.elsevier.com/locate/jssc

Original electrochemical mechanisms of $CaSnO_3$ and $CaSnSiO_5$ as anode materials for Li-ion batteries

M. Mouyane [1], M. Womes, J.C. Jumas, J. Olivier-Fourcade, P.E. Lippens *

Institut Charles Gerhardt, UMR 5253 CNRS, Equipe Agrégats, Interfaces et Matériaux pour l'Energie, Université Montpellier II, CC 1502, 34095 Montpellier Cedex 5, France

ARTICLE INFO

Article history:
Received 5 April 2011
Received in revised form
25 August 2011
Accepted 27 August 2011
Available online 3 September 2011

Keywords:
$CaSnO_3$
$CaSnSiO_5$
Li-ion batteries
Anode
^{119}Sn Mössbauer spectroscopy

ABSTRACT

Calcium stannate ($CaSnO_3$) and malayaite ($CaSnSiO_5$) were synthesized by means of a high temperature solid-state reaction. Their crystal structures and morphologies were characterized by X-ray diffraction (XRD) and Scanning Electron Microscopy; their electrochemical properties were analyzed by galvanostatic tests. The amorphization of the initial electrode materials was followed by XRD. The first discharge of the oxides $CaSnO_3$ and $CaSnSiO_5$ shows a plateau at low potential, which is due to the progressive formation of Li–Ca–Sn and/or Li–Sn alloys as shown by ^{119}Sn Mössbauer spectroscopy. The results reveal similar electrochemical mechanisms for $CaSnO_3$ and $CaSnSiO_5$ but they completely differ from those related to SnO_2.

1. Introduction

Currently commercialized Li-ion batteries work with negative electrodes based on carbon or graphite, which show good cycling performances but have limited mass and volume capacities and may be unsafe under certain conditions [1]. In order to increase the specific energy, several metals forming alloys with Li were proposed for the new generation of accumulators due to their high energy density [2].

The announcement in 1997 by Fuji photofilm of the commercialization of a more efficient and less dangerous amorphous tin-based composite oxide (ATCO) [3,4] anode directed much attention towards tin oxides such as SnO_2, $CoSnO_4$ and $CaSnO_3$ [5–7]. These oxides are considered viable due to their high capacities at low potentials as well as the pollution-free and wide availability of the raw materials and their low cost.

According to the literature bibliographic data, the energy storage in these materials is not based on the simple mechanism of a formation of Li_xSn alloys, but is rather a two step process. First, the cation Sn^{IV} is reduced to Sn^0 under simultaneous formation of Li_2O. Then, alloying takes place. Only this second process is reversible. The presence of Li_2O or other inactive materials, working as matrices in which tin can be dispersed, could buffer the volume expansion and contraction during cycling. As a result, tin oxides have attracted much attention [8,9].

In the first part of the present work, we report on the synthesis and characterization of the tin oxides $CaSnO_3$ and $CaSnSiO_5$. In the second part, we analyze the performances of these materials as a negative electrode for Li-ion batteries and compare them with those of SnO_2. A quantitative phase analysis by *ex-situ* ^{119}Sn Transmission Mössbauer Spectroscopy (TMS) at various depths of discharge and charge of $CaSnO_3$ and $CaSnSiO_5$ electrodes was carried out to this end. This analysis required the knowledge of the recoil-free fraction f of nuclear γ-absorption (Lamb–Mössbauer factor) of tin in $CaSnSiO_5$, which has been determined from a series of ^{119}Sn Mössbauer spectra recorded at various temperatures.

The main objective of the present work is to show that the electrochemical behaviors of $CaSnO_3$ and $CaSnSiO_5$ electrodes are similar, and a common electrochemical reaction mechanism valid for both oxides is proposed, which differs from that reported for SnO_2. Thus, our findings disagree with previous reports on identical processes in all three oxides [7,10].

2. Experimental

2.1. Preparation of materials

The compounds $CaSnO_3$ and $CaSnSiO_5$ were synthesized by means of a high temperature solid-state reaction. The starting

* Corresponding author.
E-mail address: lippens@univ-montp2.fr (P.E. Lippens).
[1] Present address: Laboratoire Universitaire des Sciences Appliquées de Cherbourg (LUSAC), EA 4253, Université de Caen Basse-Normandie, BP 78, 50130 Cherbourg Octeville, France.

0022-4596/$ - see front matter © 2011 Elsevier Inc. All rights reserved.
doi:10.1016/j.jssc.2011.08.038

materials used for the synthesis were: $CaCO_3$ (UCB), SnO_2 (Aldrich) and SiO_2 (Merck). For the preparation of $CaSnO_3$, stoichiometric amounts of the starting materials were mixed, ground and heated to 900 °C in air for 3 h and to 1450 °C for 14 h, followed by quenching to room temperature. For the preparation of $CaSnSiO_5$ a thoroughly ground stoichiometric mixture of the reactants ($CaSnO_3$ previously synthesized and SiO_2 (Merck)) was heated to 1300 °C in air for 12 h followed by cooling, regrinding the product, re-heating to 1300 °C for 20 h and to 1450 °C for 3 h and by cooling to room temperature. The final product was carefully ground to a fine powder.

2.2. Electrochemical tests

Electrochemical tests were carried out using a Macpile II automated system. The cells were cycled between 1.2 and 0.01 V *vs.* Li^+/Li^0 at a constant current density of 0.17 mA/cm^2 for $CaSnO_3$ and of 0.14 mA/cm^2 for $CaSnSiO_5$.

Working electrodes of these compounds were prepared by mixing the oxide powder with carbon black and polytetrafluoroethylene (PTFE) binder with a weight ratio of 80:10:10. The mixtures were then manually pressed to pellets. A lithium foil was used as the negative electrode. The electrolyte consisted of 1 M $LiPF_6$ in a 1:1:3 vol. ratio mixture of propylene carbonate (PC), ethyl carbonate (EC) and dimethyl carbonate (DMC). Whatman paper (borosilicate glass microfibre filters) was used as a separator. The cells were assembled in a glove box under dry argon atmosphere.

2.3. Analytical methods

The reaction mechanism in the $CaSnSiO_5$ and $CaSnO_3$ electrodes was analyzed *ex situ* by ^{119}Sn TMS and XRD at different depths of the electrochemical reaction. To this end the lithium insertion was stopped at various voltages. The cells were then opened inside the glove box and the electrodes were transferred to specific air-tight sample-holders equipped with radiation-transparent windows.

The phases present in all oxides were checked by powder XRD performed on a Philips X'Pert diffractometer using Cu$K\alpha$ radiation ($\lambda = 1.5418$ Å). The morphology of the powders was examined by Scanning Electron Microscopy (SEM, JEOL JSM-6300F, Field Emission Electron Microscope).

^{119}Sn Mössbauer spectra were recorded at room temperature in transmission mode on a standard instrument operated in the constant acceleration mode. The γ-ray source of ^{119m}Sn in a $CaSnO_3$ matrix had a nominal activity of 370 MBq. The velocity scale was calibrated using the magnetic sextet of a high purity iron foil as a standard spectrum and a ^{57}Co(Rh) source. Isomer shifts are given with respect to $BaSnO_3$ at room temperature. The spectra were evaluated by fitting Lorentzian profiles to the experimental data using a least-squares method. The fit quality was controlled by the classical χ^2 test.

3. Results and discussion

3.1. Structure and morphology

The compounds $CaSnO_3$ and $CaSnSiO_5$ were obtained as white powders after the solid state reaction. Fig. 1a and b shows the typical XRD patterns of the as prepared $CaSnO_3$ and $CaSnSiO_5$, respectively. All diffraction peaks in Fig. 1a can be attributed to the orthorhombic $CaSnO_3$ phase with the typical perovskite structure (JCPDS file #310312). In Fig. 1b, all reflections can be attributed to the monoclinic malayaite phase of $CaSnSiO_5$ (JCPDS file #870131) and to SnO_2, which is formed in the synthesis process as a minor impurity. The lattice parameters of the compounds, obtained by refinement with the POWDER software [11], are in good agreement with those of the JCPDS files.

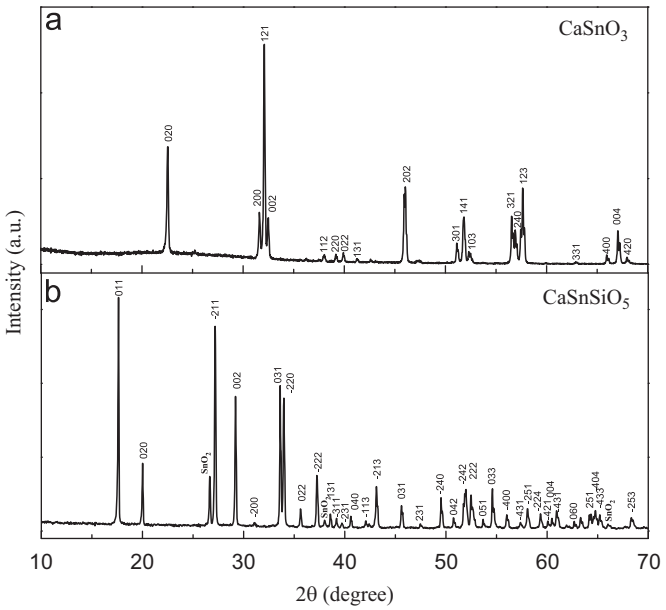

Fig. 1. Powder X-ray diffraction patterns for (a) $CaSnO_3$; (b) $CaSnSiO_5$. Cu$K\alpha$ radiation.

The morphology of the compounds analyzed by SEM is shown in Fig. 2. The $CaSnO_3$ powder presents particles of both polyhedral and spherical geometry (Fig. 2a). The average size was estimated to lie between 3 and 14 μm. $CaSnSiO_5$ consists of agglomerates of spherical particles the size of which varies from 20 to 50 μm (Fig. 2b).

Fig. 3 shows ^{119}Sn Mössbauer spectra of $CaSnO_3$ and $CaSnSiO_5$ recorded at room temperature in transmission mode. The hyperfine parameters determined by line fitting are gathered in Table 1. All isomer shifts are situated in a domain characteristic of tin in the oxidation state IV. The spectrum of $CaSnO_3$ (Fig. 3a) can be fitted by an unresolved doublet with an isomer shift and a quadrupole splitting of 0.02 and 0.18 mm/s, respectively. The spectrum obtained for $CaSnSiO_5$ (Fig. 3b) consists of a resolved doublet with a high quadrupole splitting (1.49 mm/s) and an isomer shift of −0.06 mm/s, these parameters agree with data reported in the literature [12,13]. Tin atoms in malayaite are octahedrally coordinated to oxygen atoms. The high value of quadrupole splitting reflects the inhomogeneity of the electronic environment around tin atoms due to the occupation of the next-nearest neighbor sites by both Ca and Si. The spectrum reveals also the presence of SnO_2 as an impurity, as already seen by XRD.

3.2. Galvanostatic cycling

Galvanostatic cycles of lithium cells assembled with these oxides are plotted in Fig. 4. The corresponding profile of SnO_2 is included for comparison. For the sake of clarity only the first cycle is shown in the figures and the potentials are plotted with respect to the Li^+/Li^0 counter/reference electrode. During the initial discharge a large plateau is observed for all oxides, which corresponds to the reduction of Sn^{IV}. The profile of SnO_2 is in accordance with previous works, the reduction of SnO_2 to Sn appears at about 0.9 V *vs.* Li^+/Li^0 while lithium–tin alloys are formed below 0.9 V *vs.* Li^+/Li^0 [14,15].

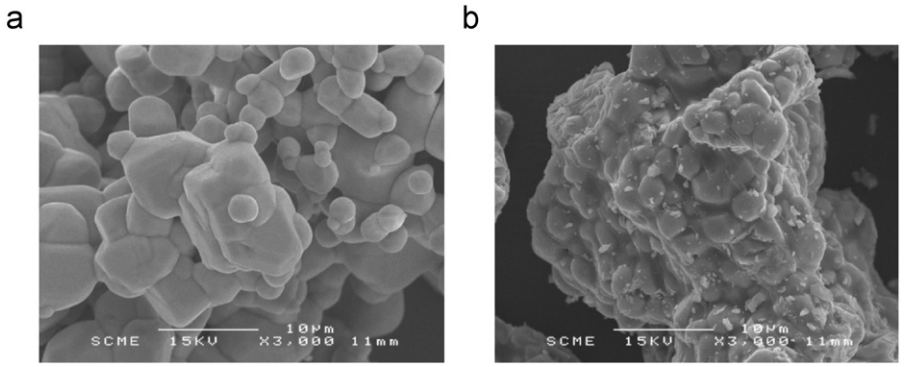

Fig. 2. SEM photographs of (a) $CaSnO_3$ and (b) $CaSnSiO_5$.

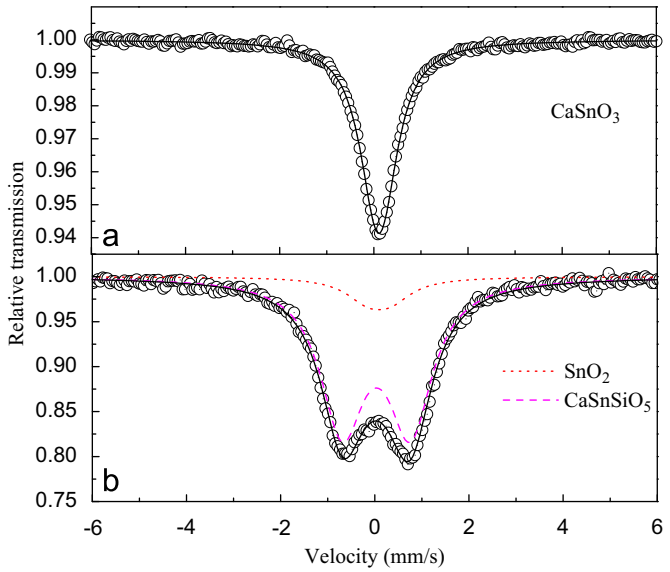

Fig. 3. Room temperature ^{119}Sn Mössbauer spectra collected in transmission mode of $CaSnO_3$ (a) and $CaSnSiO_5$ (b). Open circles denote the experimental data and the calculated spectrum is denoted by solid bold line.

Table 1
^{119}Sn hyperfine parameters of the starting materials.

Compound	δ (mm/s)	Δ (mm/s)	2Γ (mm/s)	A (%)	RA (%)	χ^2	Abs. (%)
$CaSnO_3$	0.02 (1)	0.18 (2)	0.85 (1)	100		0.49	6
$CaSnSiO_5$	−0.06 (1)	1.49 (1)	1.13 (1)[a]	88	86	0.88	21
SnO_2	−0.01 (1)	0.49 (1)	1.13 (1)[a]	12	14		

Isomer shift (δ) relative to $BaSnO_3$, quadrupole splitting (Δ), line width at half maximum (2Γ), relative contributions in the total absorption in the Mössbauer spectra (A%), relative amounts (RA%), goodness-of-fit test (χ^2) and absorption (Abs. %).

[a] Values constrained to be equal.

The first-discharge curves of $CaSnSiO_5$ and $CaSnO_3$ show an electrochemical behavior very similar to that of pure Sn-based composite materials [16,17]. The short plateau or shoulder at 0.85 V *vs.* Li^+/Li^0 in the discharge curve of $CaSnO_3$ corresponds to the formation of the solid electrolyte interphase (SEI) accompanying the irreversible reduction of the electrolyte on the surface of the carbon particles [18]. A very large plateau follows at about 0.25 V *vs.* Li^+/Li^0, which is a lower potential than that observed for SnO_2. The initial discharge capacity is 1037 mAh/g, corresponding to 8 Li per Sn. A similar potential profile is seen in the case of $CaSnSiO_5$. However, two differences are observed. The first one is the larger initial part of the curve at 0.92–0.85 V *vs.* Li^+/Li^0,

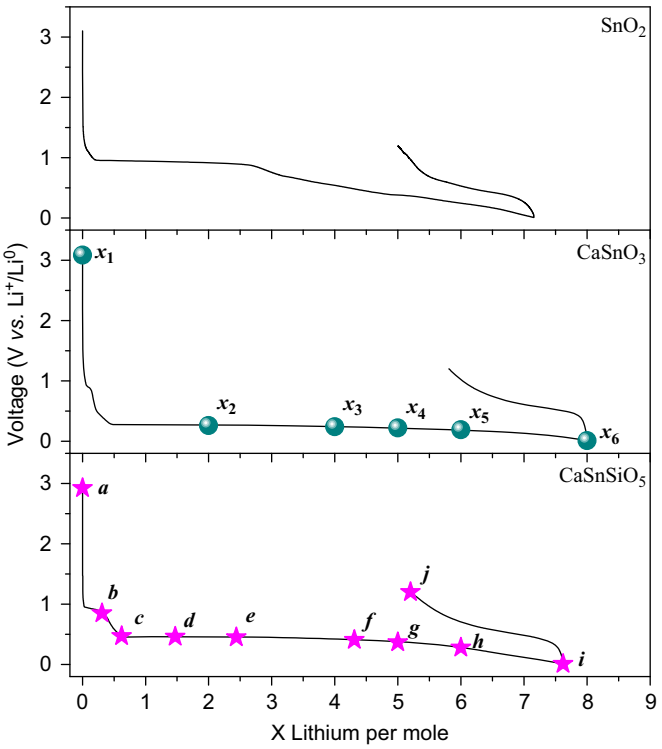

Fig. 4. Galvanostatic cycling curves of SnO_2 (C/30 rate), $CaSnO_3$ (C/30 rate) and $CaSnSiO_5$ (C/50 rate). Potential window: 0.01–1.2 V *vs.* Li^+/Li^0. Points (x_1) to (x_6) and (a) to (j) mark the samples, which were analyzed by XRD diffraction and Mössbauer spectroscopy for $CaSnO_3$ and $CaSnSiO_5$, respectively.

which corresponds to both a reduction of Sn^{IV} in the SnO_2 impurity to Sn^0 and the SEI film formation process. The second difference is the potential value of the large plateau of 0.45 V *vs.* Li^+/Li^0, which lies below that of SnO_2 but above that of $CaSnO_3$. The initial discharge capacity of 765 mAh/g corresponds to 7.6 Li per formula unit of $CaSnSiO_5$. On the first charge, a similar profile is observed for all the three oxides, showing a plateau at 0.4 V *vs.* Li^+/Li^0 for SnO_2 and higher than 0.5 V *vs.* Li^+/Li^0 for $CaSnO_3$ and $CaSnSiO_5$.

To clarify all the phenomena that occur during the charge–discharge process and to complement the galvanostatic cycling performance, the derivative curves of the first discharge process of SnO_2, $CaSnO_3$ and $CaSnSiO_5$ are plotted in Fig. 5. In SnO_2, the reduction process of Sn^{IV} to metallic tin occurs at 0.95 V *vs.* Li^+/Li^0 and the four small structures observed at 0.68, 0.57, 0.38 and 0.23 V *vs.* Li^+/Li^0 correspond to the formation of various lithium–tin alloys [19]. The first discharge of $CaSnO_3$ shows two cathodic peaks at 0.89 and 0.27 V *vs.* Li^+/Li^0 where the former can be

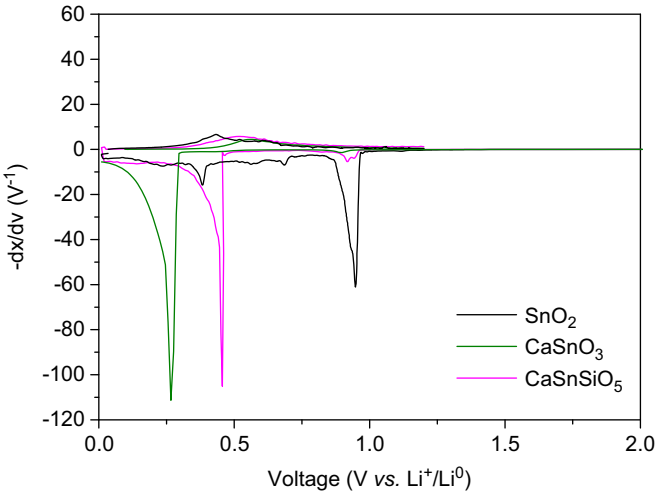

Fig. 5. Derivative curves corresponding to the first discharge/charge cycles of SnO_2, $CaSnO_3$ and $CaSnSiO_5$.

attributed to the SEI film formation process. In the case of $CaSnSiO_5$, two cathodic peaks at 0.92 and 0.52 V *vs.* Li^+/Li^0 are seen, but here the former corresponds to both the reduction of the SnO_2 impurity to tin metal and to the SEI film formation. The observation of a single intense peak for $CaSnO_3$ and $CaSnSiO_5$ in a potential domain where formation of lithium–tin alloys occurs in SnO_2 shows that the lithium insertion mechanism in these two compounds is different from that of SnO_2.

During the charging process, a small anodic peak is detected at about 0.43 V *vs.* Li^+/Li^0 for SnO_2, 0.52 V *vs.* Li^+/Li^0 for $CaSnSiO_5$ and 0.56 V *vs.* Li^+/Li^0 for $CaSnO_3$. In SnO_2, this oxidation peak is attributed to the dealloying of the Li–Sn alloys formed at the end of the discharge.

3.3. Lithium insertion mechanism

Ex situ analyses by XRD and ^{119}Sn TMS were carried out at different stages of the first discharge in order to elucidate the origin of various plateaus and to identify the electrochemical reaction mechanism of $CaSnO_3$ and $CaSnSiO_5$.

Ex situ XRD patterns of the $CaSnO_3$ and $CaSnSiO_5$ electrodes are shown in Figs. 6 and 7, respectively. For $CaSnO_3$ during the discharge a progressive loss of long-range order is observed. A broad scattering observed for the starting material in the domain 10°–30° 2θ is due to the protective film on the sample holder. Enhanced broad scattering during the reduction process reflects the amorphization of the material. At the end of the discharge only a small amount of a residual crystalline phase not reduced by lithium is observed. For $CaSnSiO_5$, the starting material (Fig. 7a: 0 Li) shows the aforementioned impurity of SnO_2. During discharge, the sample amorphization is the predominant process, revealed by a decrease in intensity of the reflections of $CaSnSiO_5$, but most of the SnO_2 impurity clearly disappears at about 0.6 Li as observed from the electrochemical potential curve. At the end of the discharge, the malayaite phase has completely disappeared and the amorphization is total, as revealed by the broad halo appearing between 10° and 30° 2θ in addition to the broad scattering from the protective film. The diffractogram of the fully recharged electrode (Fig. 7j: 5.2 Li) shows a completely amorphous material.

^{119}Sn TMS allows an identification of all tin-containing phases in a compound even in the amorphous state on the basis of their hyperfine parameters: isomer shift and quadrupole splitting. A determination of their relative amounts in multi-phased samples can be carried out by analysis of the relative areas under their

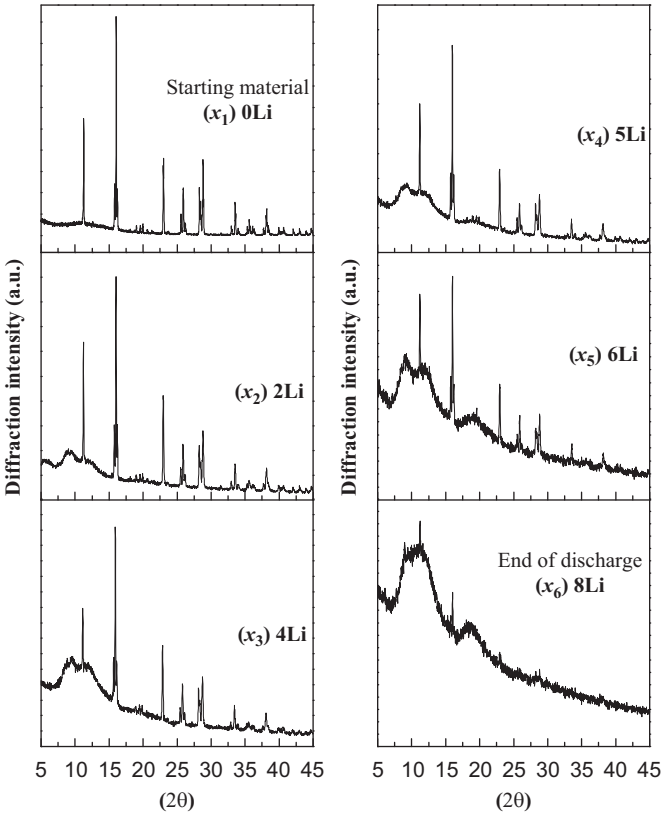

Fig. 6. *Ex situ* XRD patterns of a $CaSnO_3$ electrode recorded at different steps of the first discharge at a rate of C/30 (λ Cu$K\alpha$=1.5418 Å).

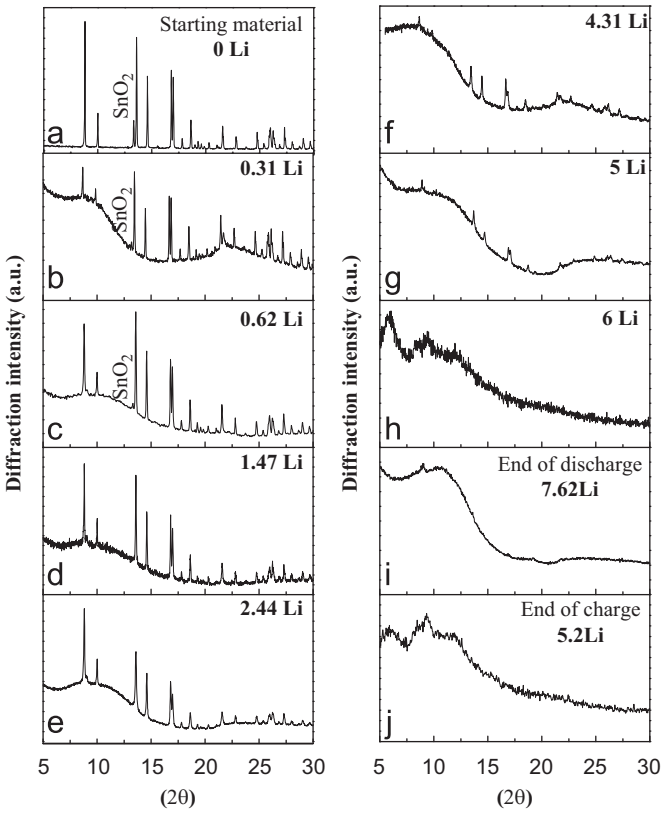

Fig. 7. *Ex situ* XRD patterns of a $CaSnSiO_5$ electrode recorded at different steps of the first discharge and end of first charge at a rate of C/50 (λ Cu$K\alpha$=1.5418 Å).

resonance absorption lines, provided the areas are corrected for the individual Lamb–Mössbauer factors f of each phase. This factor describes the ratio of recoil-free γ-absorption to the total number of absorption processes and depends on the rigidity of the tin-containing lattice at a given temperature. The more rigid the lattice, the higher will be the recoilless fraction. Literature provides room temperature f-factors for most of the phases encountered in the present study. The following data were used for the correction of the spectral areas: $CaSnO_3$: $f=0.57$ [20]; SnO_2: $f=0.56$ [21]; metallic tin: $f=0.05$ [22]; (calcium)–lithium–tin alloys: $f=0.1$ [23]. In the case of $CaSnSiO_5$, the Lamb–Mössbauer factor has been obtained by a high temperature experiment [13]. We, therefore, undertook a new determination of this factor for our purposes under lower temperature conditions.

The Lamb–Mössbauer factor within the Debye model is given by the expression [24]:

$$f(T)=\exp\left\{-\frac{3E_\gamma^2}{4Mc^2k_B\theta_D}\left[1+4\left(\frac{T}{\theta_D}\right)^2\int_0^{\theta_D/T}\frac{x\,dx}{e^x-1}\right]\right\} \quad (1)$$

where E_γ is the Mössbauer transition energy ($E_\gamma=23.9$ keV for ^{119}Sn), M the mass of the 'bare' Mössbauer atom, c the velocity of light, k_B the Boltzmann constant and θ_D the Debye temperature. The Mössbauer spectral absorption area $A(T)$ is proportional to the Lamb–Mössbauer factor within the thin absorber approximation. Thus, $A(T)$ has the same temperature dependence as $f(T)$ given by Eq. (1) and has been used to fit the absorption area for a series of ten Mössbauer spectra of $CaSnSiO_5$ recorded between 25 and 290 K in transmission geometry, the results of which are given in Table 2. The plot of $\ln(A)$ *vs.* temperature shows a typical non-linear behavior at low temperatures and rather linear variations at temperatures higher than about 200 K (Fig. 8). The fit to the experimental data shown in Fig. 8 gives $\theta_D=365$ (3) K and the room temperature Lamb–Mössbauer factor $f=0.67$ (1).

The obtained Debye temperature θ_D of 365 (3) K is lower than the value of 410 (10) K found in the literature [13]. We can explain these differences by the way our spectra were fitted in order to determine the spectral area A. Niemeier et al. [13] supposed that the width of the Sn^{IV} lines remains at a constant value of 0.89 mm/s in the whole temperature range studied. In our study, however, we can observe that the linewidth increases with the decreasing temperature as seen in Table 2. Moreover, the morphology and the particle size of the compound on which such studies are conducted can influence the values of the obtained Debye temperature.

Figs. 9 and 10 show the ^{119}Sn Mössbauer spectra of, respectively, $CaSnO_3$ and $CaSnSiO_5$ electrodes at different stages of the first discharge and at the end of the first charge for the $CaSnSiO_5$ electrode. The corresponding refined hyperfine parameters are given in Tables 3 and 4. These tables also give the effective relative amounts of the various phases after correction for their individual f-factors.

Table 2
Hyperfine parameters obtained from ^{119}Sn Mössbauer spectra of $CaSnSiO_5$ recorded in the temperature range from 25 to 290 K.

Temperature (K)	δ (mm/s)	Δ (mm/s)	2Γ (mm/s)	χ^2	Area
25	−0.01 (1)	1.47 (1)	0.95 (1)	0.56	39.42×10^{-3}
50	−0.01 (1)	1.48 (1)	0.94 (2)	0.51	38.96×10^{-3}
80	−0.01 (1)	1.47 (1)	0.93 (1)	0.85	37.71×10^{-3}
110	−0.01 (1)	1.47 (1)	0.92 (1)	0.63	36.65×10^{-3}
140	−0.02 (1)	1.47 (1)	0.92 (1)	0.58	35.59×10^{-3}
170	−0.03 (1)	1.46 (1)	0.91 (1)	0.54	34.35×10^{-3}
200	−0.03 (1)	1.46 (1)	0.92 (1)	0.57	33.42×10^{-3}
230	−0.04 (1)	1.46 (1)	0.90 (2)	0.44	31.90×10^{-3}
260	−0.05 (1)	1.45 (1)	0.90 (1)	0.54	30.94×10^{-3}
290	−0.05 (1)	1.45 (1)	0.89 (2)	0.49	29.69×10^{-3}

Isomer shifts (δ) relative to $BaSnO_3$, quadrupole splitting (Δ), line width at half maximum (2Γ) and the area under the spectra (Area) and goodness-of-fit test (χ^2).

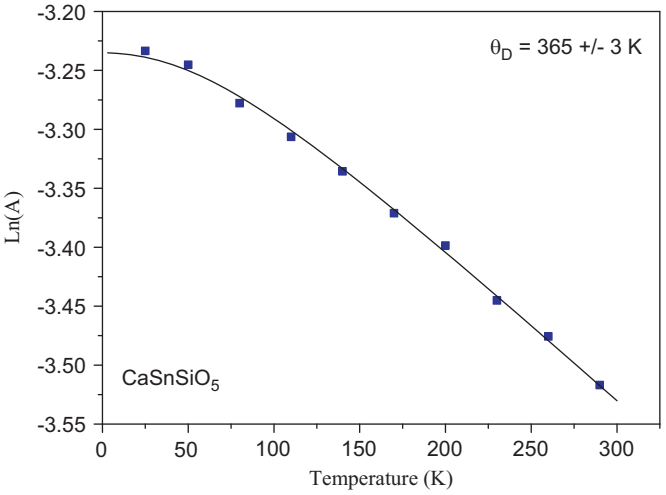

Fig. 8. Logarithmic variation of the area under the resonance absorption curve as a function of temperature of $CaSnSiO_5$. The solid line is a fit on the basis of the Debye model.

In Fig. 9 the spectrum recorded after reaction of 2 Li with $CaSnO_3$ (point x_2) can be fitted with two components of which the first, Sn^{IV} in $CaSnO_3$, represents the majority phase (67%) and the second, a doublet, represents a new phase with an isomer shift and quadrupole splitting of 2.26 and 1.31 mm/s, respectively. At 4 Li (point x_3), we note that the quantity of the new species formed at point (x_2) has increased to 66% while the proportion of $CaSnO_3$ has decreased to 34%. A further increase of this new species to 72% is observed at 5 Li (point x_4). We note here that the hyperfine parameters of the starting material remain unchanged throughout the discharge. We conclude that the reaction with lithium does not cause profound changes of the residual $CaSnO_3$ compound. The value of the isomer shift of the new phase formed during lithiation (2.26 mm/s) cannot be attributed to βSn (2.56 mm/s). Based on the correlation $\delta=f(x)$ between isomer shift δ and Li/Sn ratio x of Li–Sn alloys given in the literature (Fig. 4b in [25]) it could be attributed to a lithium–tin alloy whose composition appears to be between LiSn and Li_7Sn_3. On the other hand, the rather high values of the quadrupole splitting ($\Delta=1.1$–1.4 mm/s) as compared to pure Li–Sn alloys [25,26] suggest interactions between the active specie (Sn) and other elements like oxygen and/or calcium of the pristine material. This allows us to say that the alloys formed are likely to be modified. Similar hyperfine values have been observed during lithiation of glassy $SnB_{0.6}P_{0.4}O_{2.9}$ [27]. Finally, the rather high values of the line width at half maximum (1.2–1.6 mm/s) indicate a distribution of the Sn local environments as expected from these additional interactions.

The values of the hyperfine parameters of the electrode (x_5) are similar to those of the electrode (x_4), except for the isomer shift value of $\delta=2.04$ mm/s, which is much smaller than that of the (x_4) sample (Table 3). This shows that the lithiation process between 5 and 6 Li leads to the formation of more lithium-rich phases, which correspond to an average composition Li_5Sn_2 although the quadrupole splitting and the line width indicate again a modified structure with respect to the pure Li–Sn phases. At the end of the first discharge, after 8 reacted lithium ions, the same average composition can still be observed. A small amount of $CaSnO_3$ (2%) has not reacted with lithium. The complete conversion of the starting material might be hindered by kinetic limitations, i.e. the low diffusion rate of Li^+ into the rather large

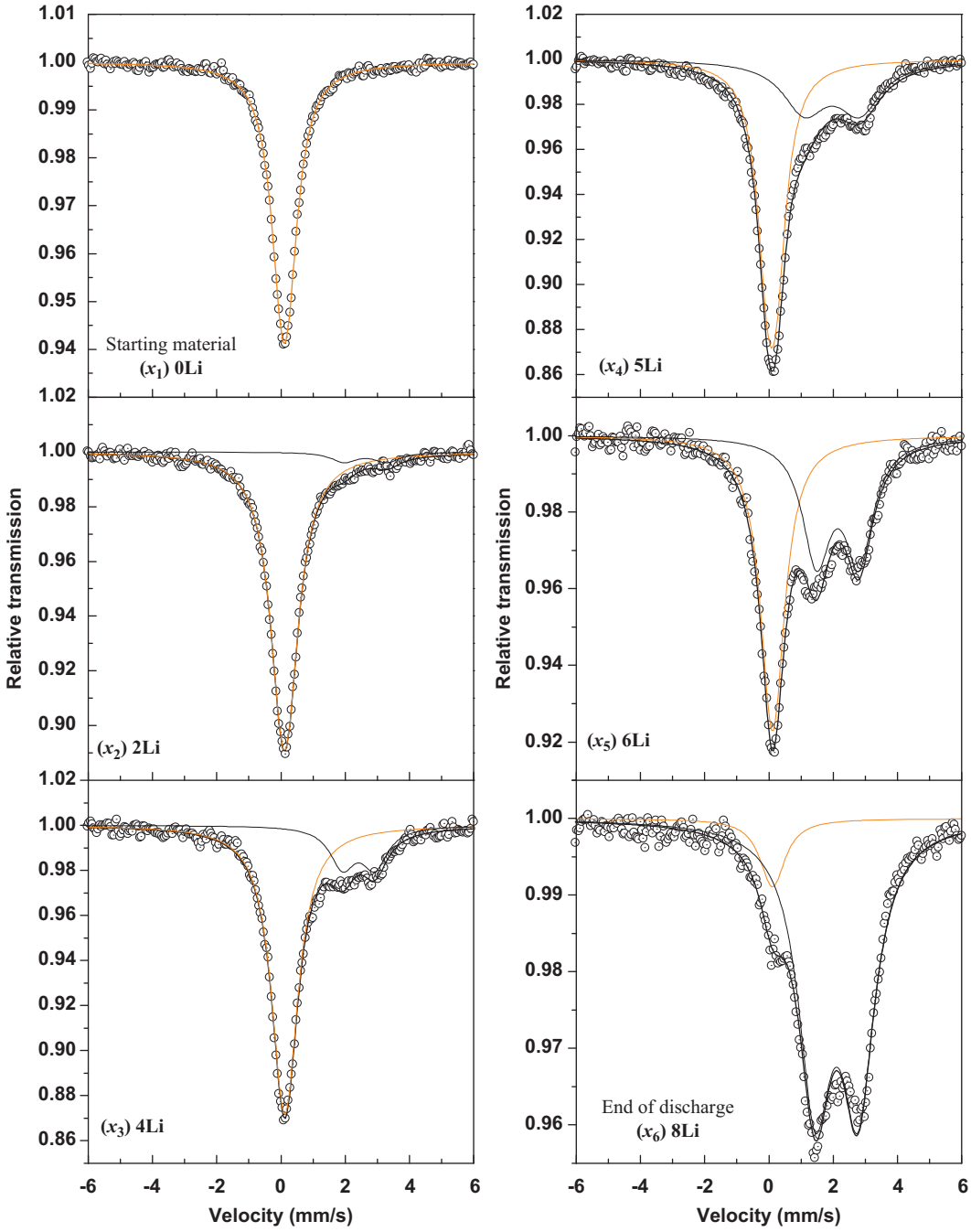

Fig. 9. *Ex situ* ^{119}Sn Mössbauer spectra at room temperature of a $CaSnO_3$ electrode recorded at different steps of the first discharge at a rate of C/30.

grains of the pristine $CaSnO_3$. It might be possible to overcome this problem by a modified synthesis procedure leading to smaller particles or by reducing the galvanostatic discharge/charge rate.

Fig. 10 shows the evolution of the Mössbauer spectra obtained during discharge/charge of $CaSnSiO_5$. The Mössbauer parameters are reported in Table 4. For the staring material (*a*), the spectrum shows 86% of $CaSnSiO_5$ and 14% of SnO_2 in agreement with the XRD data.

The analysis of spectra (*a*), (*b*) and (*c*) shows that the contribution of SnO_2 decreases. The amount of $CaSnSiO_5$ is expected to be constant. However the observed slight increase in the proportion of this compound at points (*b*) and (*c*) is due to the formation of a new Sn(0) species with a very low *f*-factor as expected from the lithiation of SnO_2. Due to its small recoilless fraction, this new Sn(0) species is not observable in the Mössbauer spectra. This contribution remains weak as compared to that of $CaSnSiO_5$ present in the electrodes. For 1.5 Li (*d*), in agreement with the XRD data, the SnO_2 sub-spectrum has completely disappeared. The first plateau at 0.9 V *vs.* Li^+/Li^0 (Fig. 4) corresponds to the reduction of tin oxide [5,28] in addition to the formation of a SEI on the carbonaceous additive. Taking into account the amount of SnO_2 in the pristine electrode evaluated from Mössbauer spectroscopy, the reduction reaction can be written as follows:

$$0.14\ SnO_2 + 0.56Li \rightarrow 0.28\ Li_2O + 0.14\ Sn(0) \qquad (2)$$

This amount of 0.56 Li is consistent with the amount of about 0.6 Li obtained between the points *a* and *c* of the potential curve (Fig. 4), which corresponds to the amount of lithium necessary to reduce SnO_2 and to form the SEI [18].

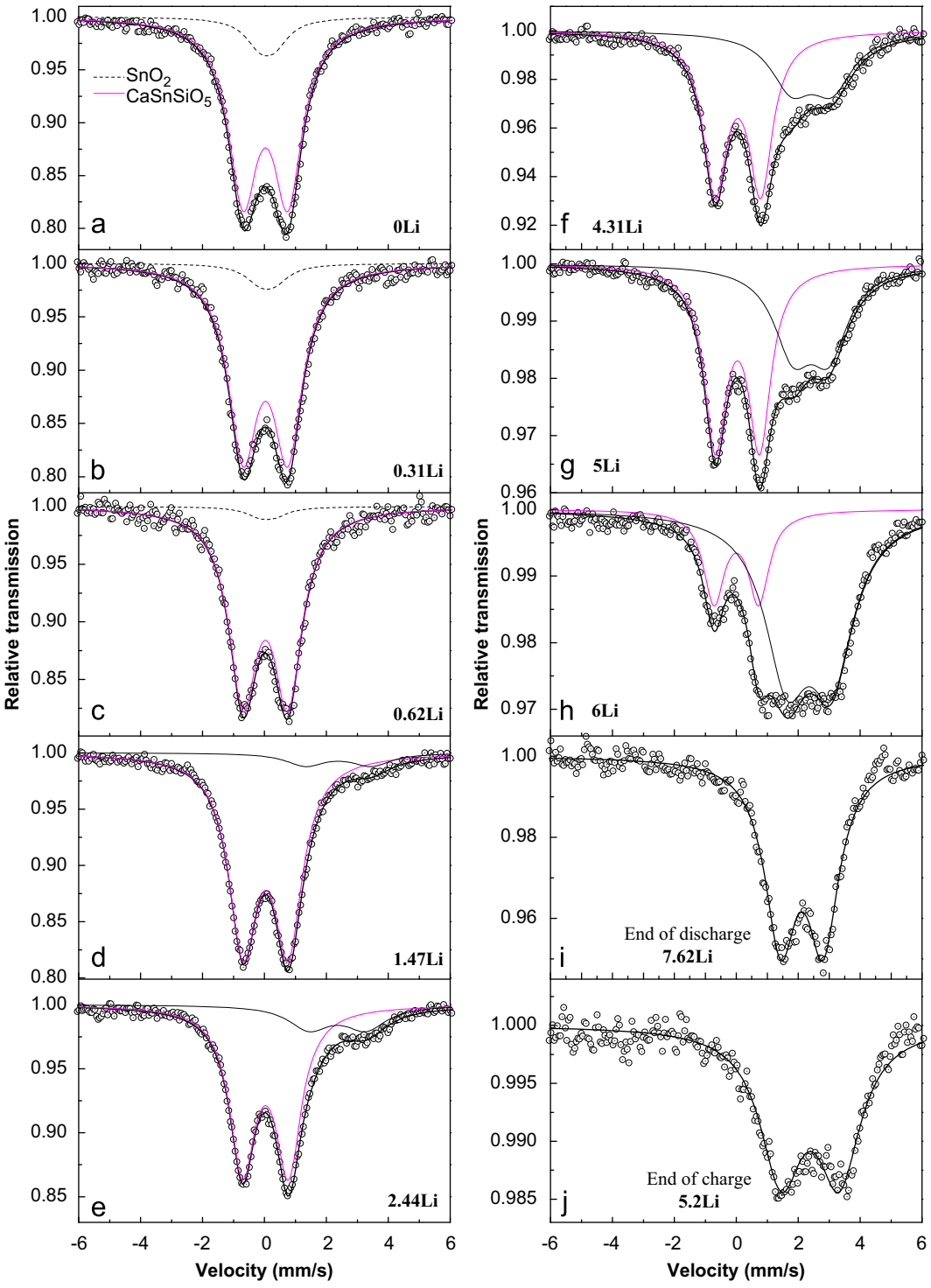

Fig. 10. *Ex situ* ^{119}Sn Mössbauer spectra at room temperature of a $CaSnSiO_5$ electrode recorded at different steps of the first discharge and at the end of the first charge at a rate of C/50.

At point (*d*), we have the formation of a new phase (26%) with an isomer shift and a quadrupole splitting of 2.47 and 1.39 mm/s, respectively. These parameters are characteristic of modified Li–Sn alloys with an average composition of about 0.5Li/Sn. The isomer shift is higher than that of the $CaSnO_3$ based electrode with 2 Li (2.26 mm/s), while the quadrupole splittings of both phases are comparable. The values of the hyperfine parameters of the electrode (*e*) are similar to those of the electrode (*d*) (Table 4), and we note that the quantity of the species previously formed increases (50%) while the proportion of $CaSnSiO_5$ decreases (50%). In the domain between 4.3 and 6 Li (between points *f* and *h*) the spectra were fitted with two components: a doublet assigned to $CaSnSiO_5$ and a second doublet at around 2.3 mm/s. The isomer shift value (2.27 mm/s) of the electrode (*h*) is lower than that of the electrode (*e*), which shows that the lithiation process starting at about 4 Li leads to the formation of a more lithium-rich composition. At this stage of the lithiation (*h*), a small amount of only 4% of $CaSnSiO_5$ remains unlithiated. At the end of the discharge, which corresponds to the reaction of 7.6 Li (*i*), the contribution of the $CaSnSiO_5$ component to the Mössbauer spectrum is not detectable. The

Table 3
Hyperfine parameters obtained from the ^{119}Sn Mössbauer spectra of a $CaSnO_3$ electrode during discharge.

Sample	Tin site	δ (mm/s)	Δ (mm/s)	2Γ (mm/s)	A (%)	RA (%)	χ^2	Abs. (%)
x_1	$CaSnO_3$	0.02 (1)	0.18 (2)	0.85 (1)	100	100	0.50	6
x_2	$CaSnO_3$	0.02 (1)	0.22 (2)	0.93 (1)	92	67	0.41	11
	"Li–Sn"	2.26 (8)	1.31 (1)	1.64 (1)	8	33		
x_3	$CaSnO_3$	0.02 (1)	0.24 (3)	0.88 (2)	75	34	0.57	13
	"Li–Sn"	2.26 (3)	1.05 (4)	1.34 (8)	25	66		
x_4	$CaSnO_3$	0.01 (1)	0.27 (2)	0.83 (1)	69	28	0.55	14
	"Li–Sn"	2.26 (8)	1.37 (2)	1.22 (4)	31	72		
x_5	$CaSnO_3$	0.02 (1)	0.19[a]	0.84 (1)	48	14	0.53	8
	"Li_5Sn_2"	2.04 (1)	1.34 (2)	1.20 (3)	52	86		
x_6	$CaSnO_3$	0.02 (1)	0.19 (1)	0.90 (9)	9	2	0.87	4
	"Li_5Sn_2"	2.02 (1)	1.34 (1)	1.26 (2)	91	98		

Isomer shift (δ) relative to $BaSnO_3$, quadrupole splitting (Δ), line width at half maximum (2Γ), relative area under the resonance curve (A%), relative amounts corrected *for* f-factors (RA%), absorption (Abs. %) and goodness-of-fit (χ^2).

[a] Values fixed in the fit.

Table 4
Hyperfine parameters obtained from the ^{119}Sn Mössbauer spectra of a $CaSnSiO_5$ electrode during discharge and charge.

Sample	Tin site	δ (mm/s)	Δ (mm/s)	2Γ (mm/s)	A (%)	RA (%)	χ^2	Abs. (%)
a	$CaSnSiO_5$	−0.06 (1)	1.49 (1)	1.13 (1)[a]	88	86	0.88	21
	SnO_2	−0.01 (1)	0.49 (1)	1.13 (1)[a]	12	14		
b	$CaSnSiO_5$	−0.06 (1)	1.45 (1)	1.14 (1)[a]	92	91	0.62	21
	SnO_2	−0.01 (1)	0.49 (1)	1.14 (1)[a]	8	9		
c	$CaSnSiO_5$	−0.06 (1)	1.45 (1)	1.10 (1)[a]	96	95	0.56	19
	SnO_2	−0.01 (1)	0.49 (1)	1.10 (1)[a]	4	5		
d	$CaSnSiO_5$	−0.05 (2)	1.46 (2)	1.12 (1)[a]	95	74	0.88	19
	"Li–Sn"	2.47 (6)	1.39 (1)	1.12 (1)[a]	5	26		
e	$CaSnSiO_5$	−0.05 (1)	1.49 (2)	1.03 (1)[a]	87	50	0.81	15
	"Li–Sn"	2.48 (3)	1.39 (1)	1.03 (1)[a]	13	50		
f	$CaSnSiO_5$	−0.04 (2)	1.47 (2)	0.93 (1)	63	21	0.59	8
	"Li–Sn"	2.35 (3)	1.30 (4)	1.65 (7)	37	79		
g	$CaSnSiO_5$	−0.05 (2)	1.43 (2)	0.88 (1)	56	16	0.58	4
	"Li–Sn"	2.32 (2)	1.16 (2)	1.51 (4)	44	84		
h	$CaSnSiO_5$	−0.09 (2)	1.44 (2)	0.82 (3)	27	4	0.8	3
	"Li–Sn"	2.27 (2)	1.44 (2)	1.72 (4)	73	96		
i	"Li_5Sn_2"	2.03 (1)	1.38 (1)	1.23 (2)	100	100	0.59	6
j	"Li–Sn"	2.29 (2)	1.88 (3)	1.67 (5)	100	100	0.75	2

Isomer shift (δ) relative to $BaSnO_3$, quadrupole splitting (Δ), line width at half maximum (2Γ), relative area under the resonance curve (A%), relative amounts corrected *for* f-factors (RA%), absorption (Abs. %) and goodness-of-fit (χ^2).

[a] Values constrained to be equal.

isomer shift of 2.03 mm/s lets to conclude on a composition close to Li_5Sn_2. The high values of both the quadrupole splitting (Δ = 1.2–1.4 mm/s) and the line width (2Γ = 1.1–1.7 mm/s) of the Li–Sn species observed during the lithiation indicate an inhomogeneous environment around the tin atoms that could be due to the presence of a variety of different ions like Ca, Si and/or O as next-nearest neighbors of tin.

During the charge process only 2.4 Li ions are extracted. The isomer shift value increases from 2.03 mm/s for the electrode at the beginning of charge (i) to 2.29 mm/s at the end of charge (j). The latter value is close to the values for the electrode at points (g) and (h). This indicates that charge process is a partial delithiation and the majority of the inserted Li ions remains trapped within the composite electrode formed during the discharge.

Fig. 11 shows the fit of the experimental data relative to the *ex situ* ^{119}Sn Mössbauer spectra at the end of discharge of both $CaSnO_3$ (dashed line) and $CaSnSiO_5$ (solid line) electrodes. This comparison shows that the composition of the species formed in both cases at the end of the discharge is similar. The results indicate that the Sn(IV) species in $CaSnO_3$ and in $CaSnSiO_5$ react with lithium by forming the same or very similar Sn(0) based alloys at the end of the first discharge. The difference observed between the two spectra (shoulder in the spectrum of the $CaSnO_3$ compound) is due to a small amount of residual $CaSnO_3$ (2%). For these materials, the relative amount of Sn(0) based alloys increases continuously with the depth of discharge (see inset on Fig. 11). This evolution is comparable for both materials indicating a very similar reaction mechanism. From our Mössbauer data, we have proved for the first time that the electrochemical reaction of lithium with $CaSnO_3$ and $CaSnSiO_5$ is different from that with SnO_2. In the latter case, the reaction takes place in two steps: an irreversible part corresponding to the reduction Sn(IV)→Sn(0), which is characterized by a long plateau at 0.9 V *vs.* Li^+/Li^0 during the first discharge, and a reversible part

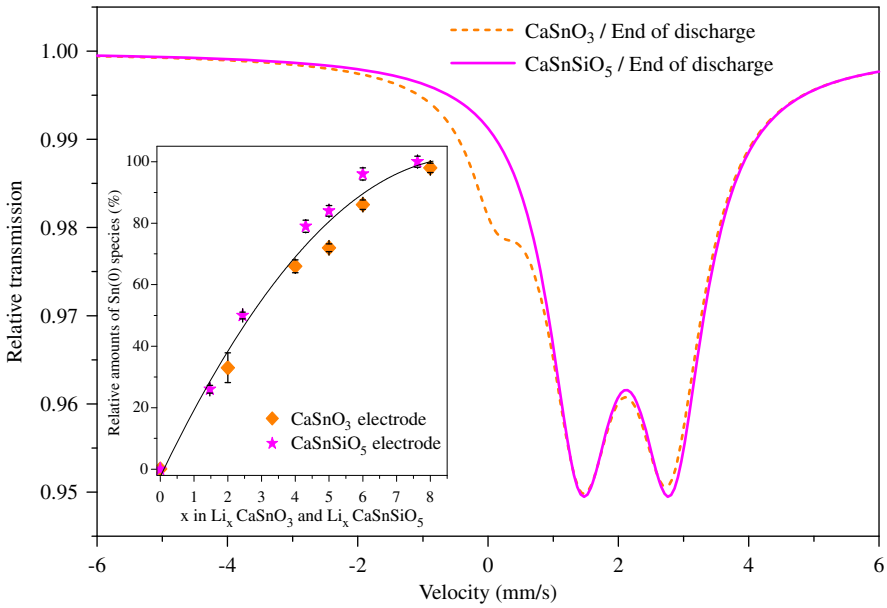

Fig. 11. Result of the fit of the experimental data relative to the *ex situ* ^{119}Sn Mössbauer spectra at the end of discharge of both $CaSnO_3$ (dashed line) and $CaSnSiO_5$ (solid line) electrodes. Inset shows the relative amounts of the Sn(0) based alloys as a function of the first discharge depth.

corresponding to the progressive formation of the Li_xSn phases [5]. Our interpretation of the Mössbauer data disagrees with previous reports on $CaSnO_3$, which proposed the following mechanism [7,10]:

$$CaSnO_3 + 4Li \rightarrow CaO + 2\ Li_2O + Sn \quad (3)$$

$$Sn + 4.4\ Li \leftrightarrow Li_{4.4}Sn \quad (4)$$

This mechanism is similar to the two-step mechanism of SnO_2 except for the formation of CaO and suggests the existence of an active Sn(0) metal like βSn. Such Sn(0) species, with expected isomer shift of about 2.5 mm/s, were never observed in our Mössbauer spectra. We propose here alternative mechanisms based on our results of XRD and ^{119}Sn Mössbauer spectroscopy.

The large irreversible capacity observed for the $CaSnO_3$ electrode (≈ 5Li) is mainly due to the irreversible formation of Li_2O because of the thermodynamical impossibility of a Li extraction from Li_2O [29] along with a small SEI formation during the first steps of the discharge process. However, this formation of Li_2O is not limited to the first part of the discharge as indicated by Eq. (3) but during all the discharge in parallel to the formation of Sn(0) species (Fig. 11, inset). The decrease of the averaged Mössbauer isomer shift of the Sn(0) species with the increasing Li content in the composite electrode indicates some changes in the composition of the formed Li–Sn(0) based species but the observed rather large values of the quadrupole splitting exclude the only formation of Li_xSn alloys. This suggests the existence of Sn–Ca and/or Sn–O bonds that increase the asymmetry of the Sn 5*p* electron density, which is at the origin of the quadrupole splitting but the former bonds are more consistent with the observed Sn(0) oxidation state than the latter bonds. In addition, the values of the isomer shift of the Ca–Sn compounds are in the range of values observed in this paper and decrease with the increasing Ca/Sn ratio: 2.1 mm/s for CaSn and 1.96 mm/s for Ca_2Sn [30]. The reported crystalline structure of LiCaSn also indicates that both Li–Sn and Ca–Sn bonds can be found within the same alloys [31]. Thus, we think that Li–Ca–Sn alloys and/or Li_xSn and Ca_xSn alloys can be assigned to the Sn(0) species detected in the Mössbauer spectra. It is difficult to distinguish these alloys because the values of the Mössbauer isomer shift are close together. Since the Ca/Sn ratio is expected to be constant in the formed Sn(0) species, the observed decrease of the isomer shift can be attributed to the increasing amount of lithium in these species during the discharge.

Because the results obtained by Mössbauer spectroscopy for $CaSnO_3$ and $CaSnSiO_5$ during the first discharge are similar, we propose that the lithiation mechanism of the malayaite is similar to that of $CaSnO_3$ except that we have also the formation of SiO_2 particles. This is confirmed by the electrochemical behavior observed for tin oxide doped with silicon. In fact, Huang et al. [32] showed that the first discharge curve of this material has a long plateau at about 0.85 V *vs.* Li^+/Li^0 proportional to the number of lithium used in the reduction reaction mentioned in Eq. (2). Thus, the electrochemical behavior is not perturbed by the silicon atoms present in the starting material. The study of the mechanism by IR spectroscopy shows the formation of SiO_2 and Li_2SiO_3 during the first discharge. On charge, the increase of the isomer shift indicates that the oxidation reaction mechanism can be explained by the dealloying reaction from Li-rich Sn(0) to Li-poor Sn(0) alloys.

Our results confirm that the mechanism obtained for $CaSnO_3$ and $CaSnSiO_5$ is particularly striking. This can be explained by the key role of the calcium atoms in the starting materials causing the low potential value of the plateau observed in the electrochemical curve. It seems that some Ca–Sn bonds are maintained during the lithiation. In contrast to this, the silicon atoms are not involved in this phenomenon and have no or very limited influence on the electrochemical mechanism.

4. Conclusion

In this paper, $CaSnO_3$ and $CaSnSiO_5$ have been prepared by direct synthesis by means of a high temperature solid-state reaction. We have shown that electrochemical reactions of Li with $CaSnO_3$ and $CaSnSiO_5$ during the first discharge are different from the two-step process observed for SnO_2. The hyperfine parameters observed by ^{119}Sn Mössbauer spectroscopy for the species formed during the lithiation process suggest the existence of Ca–Sn bonds in addition to the usual Li–Sn and Sn–Sn interactions found in the Li_xSn alloys. So, calcium is responsible

for this original mechanism. During the first discharge, the progressive transformation of the pristine materials leads to nanocomposites formed by particles of Li_2O, Sn(0) species containing Li and/or Ca atoms and SiO_2 for the malayaite.

Acknowledgements

X-ray diffraction and Mössbauer measurements have been performed at the regional technical platform "Réseau de rayons X et γ" of Université Montpellier II. The authors are grateful to the Région Languedoc Roussillon for financial support.

References

[1] W.H. Pu, X.M. He, J.G. Ren, C.R. Wan, C.Y. Jiang, Electrochim. Acta 50 (2005) 4140.
[2] A.H. Whitehead, J.M. Elliott, J.R. Owen, J. Power Sources 82 (1999) 33.
[3] Y. Idota, T. Kubota, A. Matsufuji, Y. Maekawa, T. Miyasaka, Science 276 (1997) 1395.
[4] Y. Idota, M. Mishima, Y. Miyaki, T. Kubota, J. Miyasaka, in Patent No 5618640, 1997.
[5] I. Sandu, T. Brousse, D.M. Schleich, M. Danot, J. Solid State Chem. 177 (2004) 4332.
[6] R. Alcántara, G.F. Ortiz, P. Lavela, J.L. Tirado, Electrochem. Commun. 8 (2006) 731.
[7] N. Sharma, K.M. Shaju, G.V.S. Rao, B.V.R. Chowdari, Electrochem. Commun. 4 (2002) 947.
[8] I.A. Courtney, W.R. McKinnon, J.R. Dahn, J. Electrochem. Soc. 146 (1999) 59.
[9] H. Li, X.J. Huang, L.Q. Chen, J. Power Sources 81 (1999) 340.
[10] S. Zhao, Y. Bai, W.F. Zhang, Electrochim. Acta 55 (2010) 3891.
[11] O. Lindqvis, F. Wengelin, Ark. Kemi. 28 (1968) 179.
[12] I. Ou-benmmou, H. Ahamdane, M.A.E. Raghni, F. Bensamka, A. Mosset, M.L.E. Moubtasim, J.C. Jumas, J. Eur. Ceram. Soc. 20 (2000) 2159.
[13] D. Niemeier, H. Mehner, U. Bismayer, K.D. Becker, Phys. Status Solidi 211 (b) (1999) 581.
[14] F. Belliard, P.A. Connor, J.T.S. Irvine, Solid State Ionics 135 (2000) 163.
[15] P.A. Conner, J.T.S. Irvine, J. Power Sources 97–98 (2001) 223.
[16] M. Mouyane, L. Aldon, M. Womes, B. Ducourant, J.C. Jumas, J. Olivier-Fourcade, J. Power Sources 189 (2009) 818.
[17] M. Mouyane, P.E. Lippens, M. Womes, B. Ducourant, J. Olivier-Fourcade, J.C. Jumas, Hyperfine Interact. 187 (2008) 27.
[18] H. Kim, B. Park, H.J. Sohn, T. Kang, J. Power Sources 90 (2000) 59.
[19] C.J. Wen, R.A. Huggins, J. Electrochem. Soc. 128 (1981) 1181.
[20] K.P. Mitrofanov, V.P. Gorkov, M.V. Plotnikova, S.I. Reiman, Nucl. Instrum. Methods 155 (1978) 539.
[21] G.S. Collins, T. Kachnowski, N. Benczerkoller, M. Pasternak, Phys. Rev. B 19 (1979) 1369.
[22] D.E. Conte, A. Aboulaich, F. Robert, J. Olivier-Fourcade, J.C. Jumas, C. Jordy, P. Willmann, J. Solid State Chem. 183 (2010) 65.
[23] I.A. Courtney, R.A. Dunlap, J.R. Dahn, Electrochim. Acta 45 (1999) 51.
[24] K.S. Singwi, A. Sjölander, Phys. Rev. 120 (1960) 1093.
[25] F. Robert, P.E. Lippens, J. Olivier-Fourcade, J.C. Jumas, F. Gillot, M. Morcrette, J.M. Tarascon, J. Solid State Chem. 180 (2007) 339.
[26] F. Robert, P.E. Lippens, R. Fourcade, J.C. Jumas, F. Gillot, M. Morcrette, J.M. Tarascon, Hyperfine Interact. 167 (2006) 797.
[27] F. Robert, F. Morato, J. Chouvin, L. Aldon, P.E. Lippens, J.O. Fourcade, J.C. Jumas, B. Simon, P. Biensan, J. Power Sources 119 (2003) 581.
[28] I.A. Courtney, J.R. Dahn, J. Electrochem. Soc. 144 (1997) 2045.
[29] D.W. Zhang, S. Xie, C.H. Chen, J. Electroceram. 15 (2005) 109.
[30] G. Frisch, C. Hoch, C. Röhr, P. Zönnchen, K.J.D. Becker, D. Niemeler, Z. Anorg. Allg. Chem. 629 (2003) 1661.
[31] K.C.P. Villars, J. Daams, R. Gladyshevskii, O. Shcherban, V. Dubenskyy, V. Kuprysyuk, O. Pavlyuk, I. Savysyuk, S. Stoyko, Group III Conden. Matter, vol. 43A7, Landolt-Börnstein, Springer, Berlin Heidelberg, 2009, p. 757.
[32] H. Huang, E.M. Kelder, L. Chen, J. Schoonman, J. Power Sources 81–82 (1999) 362.